THE ASTROPHYSICAL JOURNAL, 399:385–396, 1992 November 10

PRESSURE-CONFINED Lyα CLOUDS: SIMULATION RESULTS VERSUS OBSERVATIONS

GERARD M. WILLIGER
Cerro Tololo Inter-American Observatory, Casilla 603, 1353 La Serena, Chile; and Institute of Astronomy, University of Cambridge
AND
ARIF BABUL
Canadian Institute for Theoretical Astrophysics, McLennan Physical Laboratories, 60 St. George Street, Toronto, Ontario, Canada M5S 1A1; and Institute of Astronomy, University of Cambridge
Received 1992 February 6; accepted 1992 May 18

ABSTRACT

We use a hydrodynamic numerical code to study the evolution of spherical, optically thin, pressure-confined Lyα clouds in an adiabatically evolving intercloud medium. We use the results to construct the associated synthetic $d\mathcal{N}/dz$ and $d\mathcal{N}/dN_{\rm H\,I}$ distributions and compare them against observations as well as to the analytical predictions. We find that the model can largely account for the observed column density distribution with a cloud mass spectrum $d\mathcal{N} \propto M^{-\delta}\, dM$, $\delta = 1.90$; however, discrepancies are present at high column densities. In particular, the synthetic $d\mathcal{N}/dN_{\rm H\,I}$ exhibits a deficiency of clouds with $\log (N_{\rm H\,I}) \gtrsim 15.5$ and the column density distribution for a restricted redshift range about $z \approx 2.7$ has an abrupt cutoff not seen in the observations. The synthetic $d\mathcal{N}/dz$ is also inconsistent with the data and analytic predictions primarily because the redshift density declines much more rapidly at low redshifts. Both of the above effects arise as a result of the finite mass range for observable clouds, a mass range that shrinks with time. A non–adiabatically evolving ICM cannot alleviate the problems inherent in the model unless the ICM pressure evolves more rapidly than $P(z) \propto (1 + z)^5$. While effects such as inhomogeneities in the ICM can remedy the situation, a recent study argues against such a hypothesis. Aspherical systems, however, remain a possibility.

Subject headings: hydrodynamics — quasars: absorption lines

1. INTRODUCTION

The serried absorption-line forest, seen in the quasar spectra blueward of the Lyα emission, has been a subject of intensive study over the past decade. These absorption lines are generally interpreted as being due to cosmologically distributed "clouds" of highly ionized primordial gas (Sargent et al. 1980). High-resolution spectral observations indicate that these clouds are distinct entities and that the number of lines per unit redshift along a line of sight is a steep function of redshift. The processes leading to the formation of Lyα clouds are not well understood. Lyα clouds are thought to have been photoionized by intergalactic flux from quasars and galaxies, with a resulting equilibrium gas temperature of $T_c \approx 3 \times 10^4$ K for a mean intensity of ionizing flux at the Lyman limit (912 Å) of $J_\nu \approx 10^{-21}$ ergs cm^{-2} s^{-1} Hz^{-1} sr^{-1} (Sargent et al. 1980; Ostriker & Ikeuchi 1983). Of the various models put forth to explain the segregation of the clouds from the intercloud medium, two have received particular attention. The first model, proposed by Rees (1986) and elaborated upon by Ikeuchi, Murakami, & Rees (1987) suggests that the Lyα forest may be evidence for photoionized gas stably confined by the gravitational field of cold dark matter minihalos of mass $M \sim 10^9\, M_\odot$. The second model, first proposed by Sargent et al. (1980) and elaborated upon by Ostriker & Ikeuchi (1983) interprets the Lyα absorption lines as being due to intergalactic clouds confined by a hot intercloud medium. In a subsequent work, Ikeuchi & Ostriker (1986) discussed the formation of pressure-confined Lyα clouds, arguing that the clouds originate in fragmenting shells/sheets of swept-up primordial gas established by cosmological shocks.

The cosmological shocks required by the latter model could simply be the hydrodynamical consequences of gravitational collapse (Ostriker 1988; Cen et al. 1990). This possibility has not been fully explored. Alternatively, the shocks may have their origins in low energy ($E \sim 10^{60}$ ergs) explosions occurring at some early epoch. Potential "seeds" of such low energy explosions are quasars, starburst events associated with the earliest galaxies (Ostriker & Cowie 1981), and explosions of supermassive primordial stars (Carr, Bond, & Arnett 1984). For example, explosions of 10^{60} ergs occurring at $z \sim 10$ will give rise to shells of radius $R \sim 2.5$ Mpc at present (Vishniac, Ostriker, & Bertschinger 1985). In either case, the shells associated with the cosmological shocks are not massive enough to fragment gravitationally. At $z \lesssim 10$, the shells, however, are unstable to a Rayleigh-Taylor–like instability (Vishniac 1983) and will fragment into 10^6–$10^9\, M_\odot$ clouds that are in pressure equilibrium with the surrounding diffuse shock-heated gas.

Based on an analytic study of the pressure-confined clouds, Ikeuchi & Ostriker (1986) have argued that properties of such a population of clouds—such as, their redshift density and their column density distributions—closely resemble those of the observed Lyα absorption clouds. The analytic derivations, however, incorporate many simplifying assumptions, some explicit and some implicit, not all of which are justified. In this paper, we investigate the pressure-confined model for the Lyα clouds using numerical simulations, using a one-dimensional spherically symmetric Lagrangian hydrodynamical code to follow the evolution of the pressure-confined Lyα clouds. We use the results to compute realistic redshift density and redshift-integrated column density distributions for comparison with trends exhibited by Lyα clouds observed at high resolution. In § 2, we introduce the data sample of Lyα clouds identified in high-resolution observations and use the sample to determine the actual redshift density and redshift-integrated

column density distributions of the clouds. In § 3, we review the relevant aspects of the pressure-confined Lyα cloud model, highlighting the simplifying assumptions of the analytic treatment, and we discuss our simulations. In § 4, we compare the numerically computed redshift density and redshift-integrated column density distributions against analytic expectations and against the observations, and finally, in § 5, we review our findings and present our conclusions.

2. DATA SAMPLE

In order to compare the numerically computed redshift density and column density distribution of pressure-confined clouds with those exhibited by the observed Lyα clouds, we have assembled a large, high-resolution, profile-fitted data set comprising Lyα clouds identified in spectra of nine QSOs with emission-line redshifts z_Q ranging from 2.14 to 3.78 taken from a series of published sources. In order to ensure that the observed sample of Lyα clouds is complete, we restrict ourselves to lines with rest frame equivalent widths greater than $W_r = 0.2$ Å, excluding those lines which have been identified as metal lines or those Lyα absorption lines that belong to metal-line systems. We also exclude lines with H I column density log $N_{\rm H\,I} > 17.0$ with the intention of separating Lyα forest clouds from metal and Lyman-limit systems, which likely originate in H I clouds within galaxies, e.g., Bergeron (1988). Rees (1988), Blades (1988), Tytler (1988), and Sargent (1988) all indicate this H I column density to be the point beyond which metal and Lyman-limit systems dominate. However, C IV detections by Meyer & York (1987) and Lu (1991) for systems of log $N_{\rm H\,I} \gtrsim 15.5$ indicate that some or possibly even most Lyα forest systems may contain metals. Chaffee et al. (1986) conversely found very low metallicity upper limits in a Lyα cloud of log $N_{\rm H\,I} = 16.7$. This may very well blur the distinction between Lyα forest and metal systems; in this work we choose log $N_{\rm H\,I} = 17.0$ as the dividing point. We note that 3% of our sample lies in the range $15.6 \lesssim \log N_{\rm H\,I} \leq 17.0$. As no metal lines for these systems have been detected, any such contamination would have less effect on the Lyα redshift distribution, for example, than the intrinsic scatter in the data. A summary of the data sample is given in Table 1. The sample is essentially the same as that used by Webb (1987a, b). The continuum flux density f_L at the Lyman limit for Q0420−388 and Q1100−264 are taken from Babul (1991). The rest are derived from the visual magnitudes using Tytler's (1987) empirical fitting formula:

$$\log_{10} f_\nu (1 + z_Q)^{-1} = -0.4(m_V - K_V) - 20.09 \, . \qquad (1)$$

The K-corrections are estimated from Evans & Hart (1977).

We further correct our data sample for the proximity effect following the prescription of Bajtlik, Duncan, & Ostriker (1988): We only consider lines that satisfy the constraint $\omega(z) < 0.1$, where $\omega(z)$ is the relative enhancement of the ambient ionizing radiation at the cloud's redshift z due to the quasar. Adopting an $\Omega = 0$ cosmology,

$$\omega(z) = \frac{f_L}{4\pi J_L(z)} \frac{4 z_Q^2 (1 + z_Q/2)^2 (1 + z)^6}{(1 + z_Q)[(1 + z_Q)^2 - (1 + z)^2]^2} \, ; \qquad (2)$$

where $J_L(z)$ is the background ionizing flux at the Lyman limit, f_L is the QSO's continuum flux density at the Lyman limit and z_Q is the quasar redshift. We assume that $J_L(z)$ evolves as

$$J_L(z) = J_{21} \left(\frac{1 + z}{3.5} \right)^j , \qquad (3)$$

where $J_{21} = J_{L0}/10^{-21}$ ergs cm^{-2} s^{-1} Hz^{-1} sr^{-1}. Using the depletion of Lyα lines in the vicinity of quasars (the proximity effect) as an indicator of the intensity of the UV background, Bajtlik et al. (1988) estimate that $J_L = 10^{-21 \pm 0.5}$ ergs cm^{-2} s^{-1} Hz^{-1} sr^{-1} at $z = 2.5$, a value consistent with that originally determined by Sargent et al. (1980) and also consistent with the emission expected from observed quasars at that epoch (Bechtold et al. 1987). A commonly adopted value for the parameter characterizing the evolution of the UV background is $j = 4$ (Umemura & Ikeuchi 1984; Ikeuchi & Ostriker 1986), which implies a constant comoving photon density at the Lyman limit for a spectrum $J_\nu \propto \nu^{-1}$. "Measurements" of

TABLE 1

QSO ABSORPTION SPECTRUM DATA SAMPLE

QSO	z_Q	λ_r (minimum)	$\mathcal{N}$[a]	f_L[b]	m_V	Resolution[c] (FWHM km s^{-1})	Reference
Q2000−330[d]	3.783	1022.96	95	2.2	17.3	35	1
Q0207−398[e]	2.805	1084.84	37	2.5	17.15	33	2
Q0420−388	3.120	1025.83	100	3.4	16.9	33	3
Q1100−264[f]	2.143	1116.53	16	6.2	16.1	20	4
Q1158−187	2.448	1179.48	9	2.9	17.01	24	2
Q1358+113	2.571	1192.20	7	4.6	16.5	31	2
Q1448−232	2.208	1168.48	8	3.0	16.96	26	2
Q2204−573[g]	2.725	1123.03	25	2.1	17.36	33	2
Q2206−199N[h]	2.559	1022.66	35	1.7	17.33	33	5, 6
Total number of lines			332				

[a] Number of Lyα lines observed along the line of sight with $W_r \geq 0.2$ Å.

[b] QSO continuum flux density at the Lyman limit (912 Å), in units of 10^{-27} ergs cm^{-2} s^{-1} Hz^{-1} sr^{-1}.

[c] For spectra with variable resolution, value shown is the lowest resolution.

[d] Lines with rest frame wavelength $\lambda_r \in$ [1058.1, 1070.7], [1123.9, 1134.7], [1154.5, 1162.5], [1180.7, 1191.8], [1206.4, 1209.7] have been excluded.

[e] Lines with rest frame wavelength $\lambda_r \in$ [1116.4, 1163.2] have been excluded.

[f] Lines with rest frame wavelength $\lambda_r \in$ [1151.5, 1177.2] have been excluded.

[g] Lines with rest frame wavelength $\lambda_r \in$ [1144.7, 1154. 2], [1185.4, 1186.3] have been excluded.

[h] Lines with rest frame wavelength $\lambda_r \in$ [1062.7, 1123.1], [1158.9, 1198.5] have been excluded.

REFERENCES.—(1) Carswell et al. 1987; (2) Webb 1987a; (3) Atwood, Baldwin, & Carswell 1985; (4) Carswell et al. 1984; (5) Rauch et al. 1990; (6) Carswell et al. 1992.

the background flux using the quasar proximity effect suggest that $j \approx 0$ (Bajtlik et al. 1988). We shall explore both possibilities.

Past studies (Murdoch et al. 1986; Carswell et al. 1987; Bajtlik et al. 1988; Carswell et al. 1991; Lu, Wolfe, & Turnshek 1991; Rauch et al. 1992 and references therein) suggest that the distribution of Lyα clouds is adequately described by

$$\frac{d\mathcal{N}}{dz} \propto (1+z)^{\gamma} \quad \frac{d\mathcal{N}}{dN_{\rm H\,I}} \propto N_{\rm H\,I}^{-\beta} ; \tag{4}$$

where $N_{\rm H\,I}$ is the H I column density derived from W_r. For the data sample under consideration, we find that the redshift-integrated column density distribution of the clouds with $13.8 < \log (N_{\rm H\,I}) < 15.8$ is best characterized by power-law index $\beta = 1.9 \pm 0.1$, while the redshift evolution index over the epoch of observations, $1.8 \lesssim z \lesssim 3.6$, for clouds with $W_r \geq 0.2$ Å is $\gamma = 2.21 \pm 0.57$ if the background ionizing flux is characterized by $j = 0$ (i.e., nonevolving) and by $\gamma = 2.00 \pm 0.50$ if $j = 4$. For a subsample of clouds with $W_r \geq 0.3$ Å, we find that $\gamma = 1.38 \pm 0.59$ if $j = 0$ and $\gamma = 1.36 \pm 0.57$ if $j = 4$; the $d\mathcal{N}/dz$ distribution for the subsample has a tendency toward being flatter than the parent distribution. These results are consistent with the independent, higher resolution sample of Rauch et al. (1992).

3. PRESSURE-CONFINED CLOUDS

Let us consider the possibility that Lyα clouds observed along the various QSO lines of sight described in the previous section are indeed pressure-confined entities. As discussed by Ikeuchi & Ostriker (1986), the evolution of such clouds is primarily governed by the evolution of the surrounding hot intercloud medium (ICM). As the ICM pressure changes with time, the clouds will expand in order to establish or to maintain pressure equilibrium with the external medium, the rate of expansion being limited by the sound speed of the gas in the clouds. Hence, the clouds either expand in strict pressure equilibrium with the ambient ICM or are in free expansion. Adopting a spherically symmetric model for the cloud, the cross section for a line of sight to intersect a cloud of mass M and radius $R_c(M, z)$ at redshift z is $\pi R_c^2(M, z)$. The equivalent width of the resulting absorption line depends not only on the physical properties of the cloud but also on the impact parameter of the line of sight. Imposing a selection criterion similar to that used to generate the data sample, i.e., requiring the rest-frame equivalent width limit of the absorption line be greater than some $W_r^{\rm lim}$, reduces the maximum allowed value for the impact parameter from $R_c(M, z)$ to $l(M, z; W_r^{\rm lim})$ and also establishes the minimum detectable cloud mass $M_{\rm L}(z; W_r^{\rm lim})$ as defined by $l(M_{\rm L}, z; W_r^{\rm lim}) = 0$.

Assuming that the mean comoving number density of pressure-confined clouds is constant and that their mass distribution conforms to a power law $d\mathcal{N} \propto M^{-\delta} dM$, the number of clouds per unit mass observed along a line of sight is

$$\frac{\partial^2 \mathcal{N}}{\partial z\, \partial M} = \pi l^2(M, z; W_r^{\rm lim}) \Lambda_0 (1+z)^3 M^{-\delta} \frac{dl}{dz} , \tag{5}$$

where Λ_0 is a constant, $dl/dz = cH_0^{-1}(1+z)^{-2}$ is the differential proper path length for $\Omega = 0$ cosmology and $H_0 = 100\, h_0$ km s^{-1} Mpc^{-1} is the Hubble constant. Integrating the above equation over the allowed mass range for pressure-confined clouds yields the mean redshift density of clouds along a line of sight:

$$\frac{d\mathcal{N}}{dz} = \mathcal{K}_0 (1+z) \int_{M_{\rm L}(z)}^{zM_{\rm H}} dM M^{-\delta} l^2(M, z; W_r^{\rm lim}) , \tag{6}$$

where $\mathcal{K}_0 = \pi c H_0^{-1} \Lambda_0$ is a constant.

The upper limit on the mass of the pressure-confined clouds, $M_{\rm H}$, arises because clouds with masses greater than the Jeans mass at the time of their formation will not evolve in pressure equilibrium with the ICM pressure but, rather, will be unstable to gravitational collapse. The Jeans mass for a fully ionized gas cloud of primordial composition with epoch of formation z_c—z_c must be greater than 5 since the Lyα forest has been detected at redshifts as high as $z \approx 4.7$ (Schneider, Schmidt, & Gunn 1989)—is

$$M_J \approx 2 \times 10^{11} T_4^2 \tilde{P}_2(0)^{-1/2} (1+z_c)^{-p/2}\, M_\odot , \tag{7}$$

where $T_4 = T_c/10^4$ K and $\tilde{P}_2(0) = \tilde{P}(0)/10^{-2}$ cm^{-3} K. We have parameterized the evolution of the ICM pressure $\tilde{P} \equiv n_i T_i$ as

$$\tilde{P}(z) = \tilde{P}(0)(1+z)^p . \tag{8}$$

The redshift index $p = 5$ corresponds to an adiabatically evolving ICM. In the present study, we shall only explore this model. We note that the relationship in equation (7) is derived under the assumption that the total energy of the cloud is a conserved quantity; this is not so since $P\,dV$ work is either done by or on the clouds (Duncan & Ostriker 1988).

The H I column density of a cloud of mass M at redshift z intersected at impact parameter l is

$$N_{\rm H\,I}(M, z, l) = 2 \int_0^{\sqrt{R_c^2(M,z) - l^2}} dx\, n_{\rm H\,I}(\sqrt{x^2 + l^2}; M, z) . \tag{9}$$

The probability of intersecting such a cloud at impact parameter l is given by

$$P(l)dl = \frac{2\pi l\, dl}{\pi l^2(M, z; W_r^{\rm lim})} . \tag{10}$$

For clouds with a constant comoving number density and a mass spectrum $d\mathcal{N} \propto M^{-\delta} dM$, the redshift-integrated H I column density distribution of clouds observed along different lines of sight, each spanning the redshift range $[z_{\rm L}(i), z_{\rm H}(i)]$, is

$$\frac{d\mathcal{N}}{dN_{\rm H\,I}} = 2\mathcal{K}_0 \sum_i \int_{z_{\rm L}(i)}^{z_{\rm H}(i)} dz(1+z) \times \int_{M_{\rm L}(z)}^{M_{\rm H}} dM M^{-\delta} l(N_{\rm H\,I}; M, z) \left| \frac{dl}{dN_{\rm H\,I}} \right| . \tag{11}$$

The normalization factor $\mathcal{K}_0$ is the same as that in equation (6).

In order to evaluate the above distributions analytically, Ikeuchi & Ostriker (1986) adopt an idealized model for the pressure-confined clouds, i.e., the clouds are homogeneous, spherically symmetric, optically thin entities undergoing homologous expansion, and restrict themselves to redshifts $z \gtrsim 2$. At these redshifts, the clouds can be considered to be expanding in pressure equilibrium with the ambient ICM—only the most massive clouds ($M \gtrsim 10^{8.75}\, M_\odot$) experience any free expansion. Also, the heating of the gas by the background ionizing flux maintains the clouds in an approximate isothermal equilibrium in spite of the cooling effects of cloud expansion and radiative losses. The fraction of neutral hydrogen in

such clouds is $\chi(z) = 0.138(3.5)^j T_4^{-3/4} J_{21}^{-1} (1+z)^{-j} n_{\rm H}(z)$. To compute the probability of intersection a cloud along a line of sight, Ikeuchi & Ostriker (1986) use the full cross-sectional area of the cloud $\pi R_c^2(M, z)$, with each cloud of mass M being assigned a unique H I column density, its area-averaged column density,

$$N_{\rm H\,I} = \tfrac{4}{3}\chi(z) n_{\rm H} R_c(M, z) \; ; \tag{12a}$$

$$R_c(M, z) = [3M/4\pi\mu n_{\rm H}]^{1/3} = 0.269 M^{1/3} T_4^{1/3} \tilde{P}_2(0)^{-1/3} (1+z)^{-p/3} \text{ kpc} . \tag{12b}$$

Restricting themselves to clouds with column densities above some detection threshold $N_{\rm H\,I}^{\rm lim}$ or equivalently, to clouds with masses greater than

$$M_{\rm L}(N_{\rm H\,I}^{\rm lim}, z) = 1.81 \times 10^{19} (3.5)^{-3j} J_{21}^3 \, T_4^{29/4} \tilde{P}_2(0)^{-5} \times (1+z)^{-5p+3j} \left(\frac{N_{\rm H\,I}^{\rm lim}}{10^{14} \text{ cm}^{-2}} \right)^3 M_\odot , \tag{13}$$

and assuming that the upper bound for the mass of the pressure-confined clouds is unimportant, Ikeuchi & Ostriker (1986) found that the redshift-integrated column density and the redshift density distributions of the pressure-confined clouds are

$$\frac{d\mathcal{N}}{dN_{\rm H\,I}} \propto N_{\rm H\,I}^{-\beta} \quad \beta = 3\delta - 4 \quad N_{\rm H\,I} \geq N_{\rm H\,I}^{\rm lim} \; ; \tag{14a}$$

$$\frac{d\mathcal{N}}{dz} \propto (1+z)^{\gamma} \quad \gamma = (5\delta - 9)p - (3\delta - 5)j + 1 . \tag{14b}$$

According to these relationships, the data set examined in the previous section ought to be consistent with a pressure-confined cloud model with $\delta \approx 1.93$; given our assumption that the ICM is evolving adiabatically ($p = 5$), we expect the two models, $j = 0$ and $j = 4$, to bracket the observed redshift density of the clouds with $\gamma = 3.25$ and $\gamma = 1.09$, respectively.

Various authors (Ikeuchi & Ostriker 1986; Ikeuchi 1987; Ostriker 1988; Duncan & Ostriker 1988) have argued in favor of the pressure-confined model for the Lyα clouds on the grounds that the column density distribution and the redshift density can naturally account for the observed trends if the mass spectrum of the clouds as well as indices p and j are judiciously chosen. The power-law distributions, however, do not arise naturally but are the result of various simplifying assumptions, the validity of which have never been studied in detail. For example, the right-hand side of equation (14b) should be multiplied by $F(z) = 1 - [M_{\rm H}/M_{\rm L}(z)]^{-(\delta - 5/3)}$, but this factor has been ignored on the grounds that $M_{\rm H}/M_{\rm L}(z) \gg 1$ (for $\delta > 5/3$) over the redshift range of interest [i.e., $F(z) \approx 1$]. The validity of this assumption depends strongly on the choice for the indices p and j.

In order to explore the pressure-confined model for the Lyα clouds in greater detail, we study the evolution of the clouds with a hydrodynamical code (Williger 1991). Consequently, we are able to relax many of the assumptions incorporated in the analytic derivations of $d\mathcal{N}/dN_{\rm H\,I}$ and $d\mathcal{N}/dz$. In particular, we can allow for variations in the column density for a given cloud according to the line-of-sight impact parameter and can allow for clouds that are expanding in pressure equilibrium with the ambient ICM as well as those in free expansion. We also specifically take into account the finite upper mass cutoff for pressure-confined clouds. Finally, the simulations allow us to construct absorption-line profiles for each impact parameter and, hence, to determine the associated rest frame equivalent width W_r and the velocity parameter $b \equiv 2^{1/2} \sigma$ using Voigt profile calculations. In this way, we are able to subject the simulated profiles to the same selection criteria as that applied to the observational data set; i.e., we consider only simulated profiles with $W_r \geq W_r^{\rm lim}$, where $W_r^{\rm lim}$ corresponds to the threshold rest frame equivalent width of the Lyα clouds in the observed data set. We note that the equivalent width limit is a natural quantity for defining an observational data sample because W_r of an absorption line can be directly measured; on the other hand, analytic relationships for $d\mathcal{N}/dz$ rely on detection limits defined by a threshold H I column density, which can be determined only indirectly by modeling the absorption-line profile.

The clouds in our simulations are spherically symmetric and assumed to be optically thin. We adopt a primordial composition of 90% hydrogen and 10% helium by number for the gas in the clouds; the neutral fractions for H I, He I, and He II are computed at each time step using expressions given by Black (1981); we allow for the degree of ionization of the gas to depart from that required by ionization equilibrium considerations when the recombination time scales become long. We assume that the spectrum of the ionizing background flux at frequencies greater than the $\nu_{\rm L}$, the Lyman limit frequency, is $J_\nu \propto \nu^{-1}$. We establish the clouds at $z_c = 6$; at formation, we adopt a uniform density profile for gas distribution in the clouds and require the clouds to be in pressure equilibrium with the surrounding ICM, i.e., $n_c(z_c) = \tilde{P}(z_c)/T_c(z_c)$. On the basis of theoretical and observational contraints, the best estimate for the ICM pressure is $\tilde{P}(0) \approx 10^{-2\pm0.2}$ cm^{-3} K (Ostriker & Ikeuchi 1983)[1]; we adopt $\tilde{P}(0) = 2 \times 10^{-2}$ cm^{-3} K. The initial temperature of the gas in the clouds is set to $T_c(z_c) = 3 \times 10^4$ K; however, the gas falls quickly to its equilibrium temperature of $T \approx 2.6 \times 10^4$ K, in agreement with the findings of Umemura & Ikeuchi (1984). We also assume that the clouds are initially in homologous expansion where the expansion velocity of the cloud surface at radius R_c corresponds to Hubble flow: $V_c(z_c) = H(z_c) R_c(M, z_c)$. The subsequent evolution of the thermal and dynamical variables are not artificially constrained; in particular, the cloud density profile is not constrained to remain uniform at later times. We do note, however, that we neglect the effects of thermal conduction on the evolution of the clouds.

In order to test the hydrodynamic code, we evolved 10^6, 10^7, 10^8, and 10^9 $M_\odot$ clouds in a $p = 5$, $j = 4$ environment and compared the evolutionary tracks of individual cloud parameters, such as the mean density, the mean column density, the surface expansion velocity, and the cloud temperature, against those discussed by Umemura & Ikeuchi (1984) and Ikeuchi & Ostriker (1986). The results are almost identical.

Apart from testing the numerics of the code, we were particularly concerned about the effect of the initial expansion velocity on the state of the clouds during the epoch of observation $1.8 \lesssim z \lesssim 3.6$, the redshift range over which we intended to compare the simulation results for $d\mathcal{N}/dz$ and $d\mathcal{N}/dN_{\rm H\,I}$ against observations. The initial surface expansion velocity of $V_c = H(z_c) R_c$ that we have imposed is lower than that required to maintain pressure equilibrium. The evolution of the test clouds reveal that small ($M < 10^8$ $M_\odot$) clouds, the clouds least

[1] Note that Ostriker & Ikeuchi (1983) define pressure $\tilde{P}(0)$ using proton densities.

affected by self-gravity and with relatively small sound crossing time, adjust their expansion rate and reestablish pressure equilibrium in a very short period of time; the expansion velocity rises steeply and converges onto the "equilibrium" expansion velocity after a series of high-frequency, strongly damped oscillations. The recovery period for the massive clouds $M \sim 10^8$–$10^9\ M_\odot$ extends over a longer period of time; the oscillations in the surface expansion velocity persist even at $z \approx 4$, although the amplitude of the oscillations is only approximately 3 km s^{-1} and declining. To investigate the effect of initial expansion velocity further, we explored the consequences of starting the clouds with differential initial velocities: $V_c = (5/3)H(z_c)R_c(z_c)$ and $V_c = \frac{1}{2}H(z_c)R_c(z_c)$. We specifically focused on the massive ($M = 10^9\ M_\odot$) clouds, the clouds in which the effects of the initial velocity persist the longest. The evolution of the surface expanson velocity is shown in Figure 1 as is the evolution of one of the internal parameters of the cloud, the central equivalent width (i.e., the equivalent width of a cloud observed at impact parameter $l = 0$). The trajectories of the internal parameters of the clouds with initial velocities different from the Hubble flow exhibit more pronounced oscillations. Comparing the three cases at $z = 4$, we find that the mean column density spans the range 1.3–2 × 10^{15} cm^{-2} and that the maximum difference in the central equivalent width limit is $\Delta W_r = 0.046$ Å. In comparison with the observational errors, these differences are not significant (Carswell 1990), and, of course, these differences decrease with time. Therefore, the internal state of the pressure-confined clouds during the epoch of observation is relatively insensitive to the initial surface expansion velocity of the cloud. Umemura & Ikeuchi (1984) also drew similar conclusions.

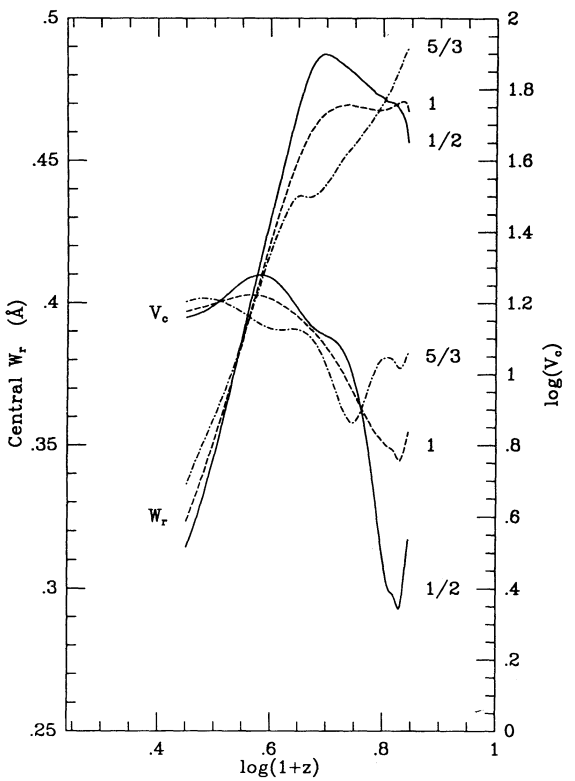

FIG. 1.—The evolution of the surface expansion velocity (V_c in km s^{-1}) and the central equivalent width (W_r in Å) for $M = 10^9\ M_\odot$ clouds in an environment where the ICM pressure evolves as $P(z) \propto (1 + z)^5$ and the UV background evolves as $J_\nu \propto (1 + z)^4$. The three sets of curves correspond to clouds starting with initial surface expansion velocity $V_c/H(z_c)R_c = 5/3$ (*dot-dash*), 1 (*dashed*), and 1/2 (*solid*).

As noted previously, in simulations of the pressure-confined clouds used to compute the synthetic $d\mathcal{N}/dN_{\rm H\,I}$ and dN/dz distributions, we consider only clouds immersed in an adiabatically evolving ICM ($p = 5$) but explore two different models for the evolution of the UV background characterized by $j = 0$ and 4. The $p = 5, j = 4$ model ("the standard model") is the one advocated by Ikeuchi & Ostriker (1986). According to analytic considerations, this model ought to be able to account for the trends exhibited by the observed Lyα clouds if the cloud mass spectrum is characterized by $\delta \approx 2$. We also consider clouds immersed in a nonevolving ($j = 0$) UV background because an analysis of the proximity effect by Bajtlik et al. (1988) suggests that the flux intensity of the actual UV background is approximately constant over the redshift range $1.8 \lesssim z \lesssim 3.8$. We note that according to the analytic relationships, the $p = 5, j = 4$ model coupled with the value of the mass spectrum index δ required to match the observed $d\mathcal{N}/dN_{\rm H\,I}$ ought to yield a slightly flatter $d\mathcal{N}/dz$ distribution than observed, while the $p = 5$, $j = 0$ model ought to exhibit a slightly steeper redshift density.

The clouds in our simulations span the mass range $2.75 \leq \log\ (M/M_\odot) \leq 9.25$ with mass resolution of $\Delta \log\ (M/M_\odot) = 0.25$. The upper limit is established by the requirement that the clouds ought not be collapsing during the epoch of observations; such clouds would not be "pressure-confined." Our upper mass limit for the clouds is a factor of 4 smaller than the Jeans mass condition given in equation (7); we found that clouds in our simulations with mass $M = 10^{9.75}\ M_\odot$ collapsed rapidly while those with mass $M = 10^{9.50}\ M_\odot$ experienced a more gradual collapse, but collapsed nonetheless. The lower mass limit has no physical origin and is simply chosen to ensure that we have considered the smallest clouds that can yield absorption features with $W_r \geq 0.2$ Å at any time during the epoch of observation. Cowie & McKee (1977), however, argue that there is indeed a physically motivated lower bound on the range of allowed masses of Lyα clouds established by the requirement that the clouds survive evaporation due to thermal conduction of heat from the hot ambient ICM. For the initial conditions adopted in the present study, this lower bound is $M_{\rm evp} \approx 10^5 \tilde{n}_6(0)^{-15/4}\ h^{-3/2}\ M_\odot$, where $n_6(0) \equiv n_i(0) \equiv n_i(0)/10^{-6}$ cm^{-3}, while our adopted lower bound is some three orders of magnitude smaller. In a test simulation, the central equivalent width limit of a $10^4\ M_\odot$ cloud subject to thermal conduction decreased from its initial value of $W_r = 0.4$ Å to an equivalent width less than 0.2 Å, our detection threshold, by $z = 5.94$; with the heat conduction suppressed, the same cloud simulation exhibited a very small change in the central equivalent width over the same period. In the present study, we have chosen to ignore the lower bound established by evaporation considerations because $M_{\rm evp}$ depends sensitively on uncertain quantities, such as n_i, and furthermore, even a dynamically insignificant tangled magnetic field can greatly modify the value of $M_{\rm evp}$.

4. RESULTS

Using the evolutionary information for the simulated clouds according to the prescription given in equations (6) and (11), we compute the synthetic $d\mathcal{N}/dz$ and $d\mathcal{N}/dN_{\rm H\,I}$ distributions for the pressure-confined Lyα clouds model with three choices for the cloud mass spectrum characterized by $\delta = 1.87$, 1.90,

and 1.93. According to the analytic relationship given in equation (14a), these values for δ ought to yield $d\mathcal{N}/dN_{\rm H\,I}$ distributions that range from being compatible with our data to those with β index as low as 1.6. The computed $d\mathcal{N}/dz$ and $d\mathcal{N}/dN_{\rm H\,I}$ distributions can be directly compared to the observations once they have been appropriately normalized (establish the value of $\mathcal{N}_0$ in eqs. [6] and [11]). We normalize the distributions by demanding that the total number of pressure-confined clouds in the column density range $14.2 \leq \log(N_{\rm H\,I}) \leq 15.2$ be equal to the number observed.

4.1. H I *Column Density Distribution*

In Figure 2, we display the observed column density distribution juxtaposed alongside the mean redshift-integrated column density distribution for the pressure-confined clouds along a line of sight. Figure 2*a* corresponds to the clouds immersed in a background flux whose redshift evolution is characterized by $j = 0$, while Figure 2*b* illustrates the results for the "standard" $j = 4$ model. First, we note that the curves corresponding to the three different mass spectra are, for all practical purposes, indistinguishable over the column density range under consideration. Second, the model distributions in both plots (Figs. 2*a* and 2*b*) fit the observations very well for column densities $\log(N_{\rm H\,I}) \lesssim 15.5$; however, the two become increasingly discrepant toward high column densities, with the synthetic distributions tending to steepen. The decline in the number of pressure-confined clouds at high column densities is more dramatic in the standard model than in the $j = 0$ case. For example, the power-law index of the column density distribution for clouds with mass spectrum characterized by $\delta = 1.90$ and immersed in a background UV flux evolving according to the $j = 0$ (4) model is $\beta = 1.66$ (1.77) over the column density range $13.8 < \log(N_{\rm H\,I}) < 14.8$, steepening to $\beta = 2.48$ (3.17) over the column density range $14.8 < \log(N_{\rm H\,I}) < 15.8$. Based on simple analytic considerations, we would have expected a single power-law column density distribution (eq. [14b]) with index $\beta = 1.70$, regardless of the value of the flux evolution parameter j. At low column densities, the synthetic and the analytically derived column density distributions are consistent with each other, but at high column densities, the discrepancy between the two is significant.

To determine the cause of the curvature and the j-dependence of the redshift-integrated $d\mathcal{N}/dz$ for pressure-confined clouds, we plot, in Figure 3, the observed and the synthetic $d\mathcal{N}/dN_{\rm H\,I}$ distributions for clouds in the redshift range $2.6 < z < 2.8$; this is the redshift bin with the largest number of Lyα clouds. The plots again show that the model

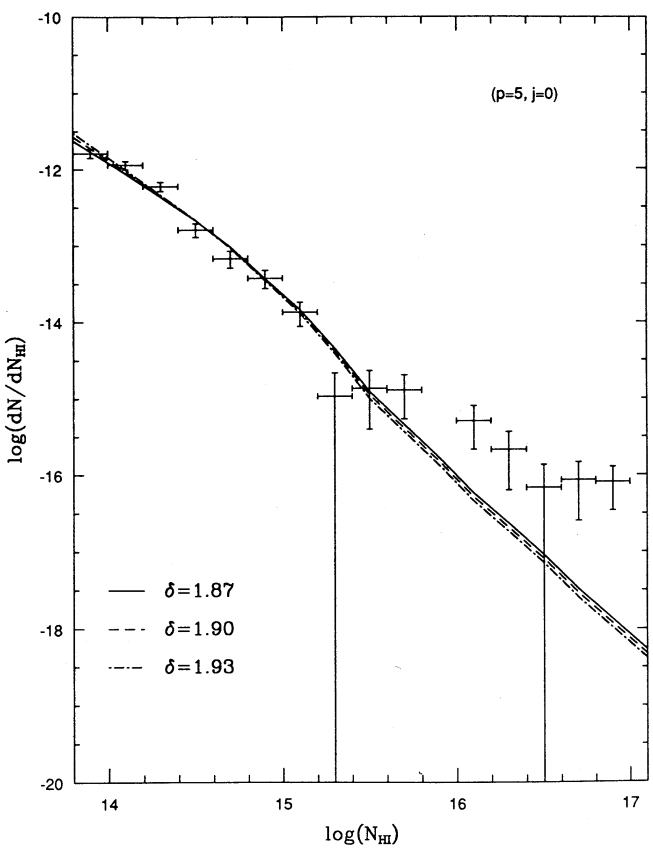

FIG. 2*a*

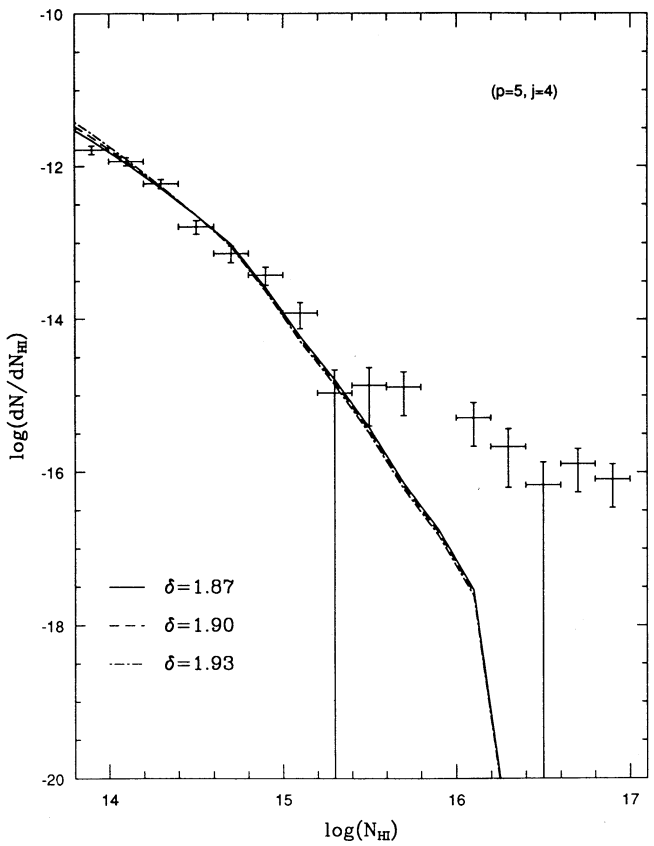

FIG. 2*b*

FIG. 2.—H I column density distribution of the observed clouds integrated over the redshift range $1.7 < z < 3.6$ juxtaposed with the curves corresponding to the redshift-integrated $d\mathcal{N}/dN_{\rm H\,I}$ for the pressure-confined clouds. The three curves correspond to clouds with mass spectra characterized by $\delta = 1.87$ (*solid curve*), $\delta = 1.90$ (*dashed curve*), and $\delta = 1.93$ (*dot-dash curve*). The error bars represent 1 σ errors for the observations. The model curves are normalized so that the total number of clouds in the column density range $14.2 \leq \log(N_{\rm H\,I}) \leq 15.2$ is equal to the observed number of clouds. In (*a*), we plot the $d\mathcal{N}/dN_{\rm H\,I}$ for clouds in the $j = 0$ model, and (*b*) illustrates the distribution for the $j = 4$ model.

$d\mathcal{N}/dN_{\rm H\,I}$ distributions are declining much more rapidly than the observed distribution at column densities $\log(N_{\rm H\,I}) \gtrsim 15$. For $\delta = 1.90$ mass spectrum and UV flux evolution parameter $j = 0$ (4), $\beta = 1.36$ (1.71) over the range $13.8 < \log(N_{\rm H\,I}) < 14.6$, while $\beta = 2.48$ (3.09) over the column density range $14.6 < \log(N_{\rm H\,I}) < 15.6$. The decline in the number of synthetic high column density observations reflects the decreasing probability for a line of sight to intersect clouds with mass $M \geq M_L(z, N_{\rm H\,I})$ at appropriate impact parameter $l(M, z; N_{\rm H\,I})$ (cf. eq. [10]). As $N_{\rm H\,I}$ increases, both the mass range $M_L(z, N_{\rm H\,I}) \leq M \leq M_{\rm H}$ of observable clouds and the range of values spanned by l decreases. As M_L approaches $M_{\rm H}$, the upper limit for the mass of the pressure-confined clouds imposed by the Jeans condition (cf. eq. [7]), the number of clouds giving rise to the desired column density as well as the mass-averaged cross sectional area for observing it drops steeply to zero. Indeed, the rapid decline of simulated clouds at high column densities in Figure 3*b* is punctuated by the lack of any clouds with column densities greater than $\log(N_{\rm H\,I}) \approx 17.8$. The sensitivity of the synthetic $d\mathcal{N}/dN_{\rm H\,I}$ to the value of j, culminating in the different values of the maximum column densities for the $j = 0$ and the $j = 4$ cases, is also the consequence of a cap on the masses of pressure-confined clouds. The highest column density observations, in the pressure-confined model, are due to the most massive clouds at high redshifts. An upper bond in mass translates into an upper limit for column density. The value of this maximum H I column density, however, is dependent on the intensity of the UV background; at redshifts $z \gtrsim 2.5$, the $j = 4$ UV flux is more intense than the $j = 0$ flux. Hence, the maximum H I column density in the $j = 0$ scenario is greater than in the $j = 4$ case. As a result of the steepening and truncation at high column densities, the $d\mathcal{N}/dN_{\rm H\,I}$ distributions for the pressure-confined models are inconsistent with the observations; the latter does not exhibit any breaks. It may be possible that there is an onset of contamination by metal absorption systems at $\log N_{\rm H\,I} \gtrsim 15.5$ where the model $d\mathcal{N}/dN_{\rm H\,I}$ distribution exhibits a shortfall in comparison against the data (e.g., Meyer & York 1987; Lu 1991), but it would have to be rather contrived to produce no associated slope change in $d\mathcal{N}/dN_{\rm H\,I}$, especially at randomly chosen redshifts.

The above problems associated with the upper bound on the mass of pressure-confined clouds can be alleviated if the assumption that the ICM pressure is homogeneous is relaxed and regions with pressure inhomogeneities of a few orders of magnitude allowed for (Baron et al. 1989). This is not unrealistic considering that $\tilde{P}$ is known to range from 10^{-2} cm^{-3} K in the ICM (Ostriker & Ikeuchi 1983) to $\gtrsim 10^5$ cm^{-3} K in the central regions of clusters of galaxies. High column density observations could then be associated, to a large degree, with clouds in high-pressure environments. The presence of such regions, however, ought to produce groups of clouds with larger than average equivalent widths along the lines of sight; Webb & Barcons (1991) have searched for such groups and,

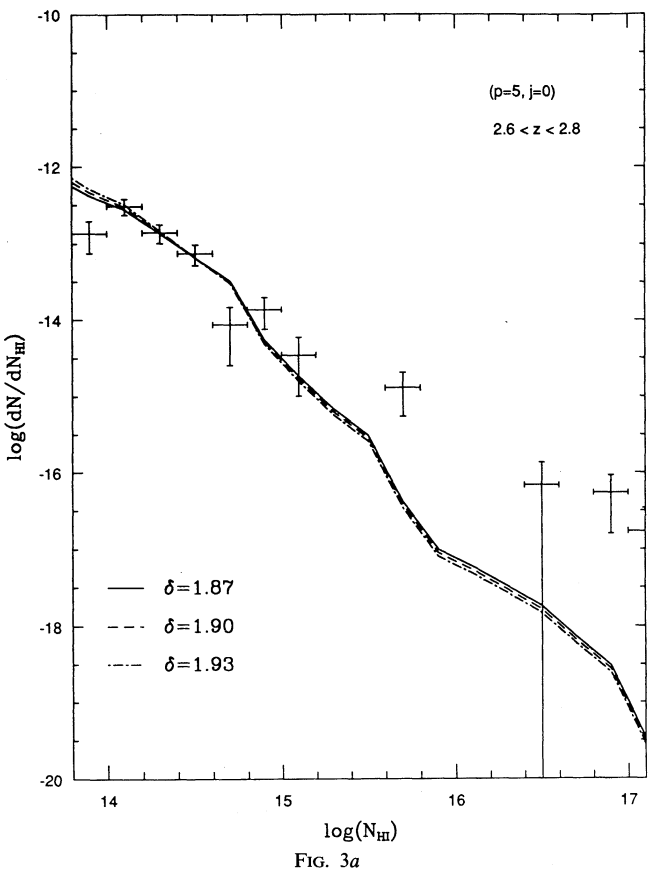

FIG. 3*a*

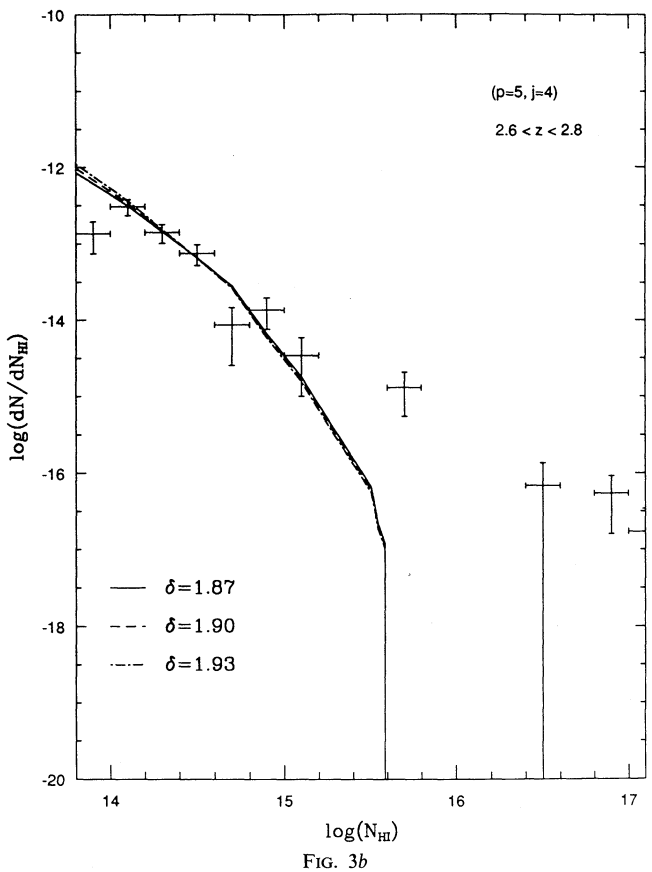

FIG. 3*b*

FIG. 3.—Column density distribution of the observed clouds in redshift range $2.6 < z < 2.8$ juxtaposed with the curves corresponding to the $d\mathcal{N}/dN_{\rm H\,I}$ for the pressure-confined clouds at the same redshifts. The error bars represent 1 σ errors for the observations. In (*a*) we plot the $d\mathcal{N}/dN_{\rm H\,I}$ for clouds in the $j = 0$ model, and (*b*) illustrates the distribution for the $j = 4$ model. We note that the synthetic curves tend to steepen prior to an abrupt cutoff.

finding none, have been able to limit the magnitude of the pressure inhomogeneities in the ICM to $\Delta P/P \lesssim 0.17$ if the observed clouds are pressure-confined entities. Alternatively, the problems resulting from the upper bound on the mass of the clouds may be resolved if the clouds are significantly aspherical (Baron et al. 1989).

4.2. *Redshift Density Distribution*

In Figure 4, we plot the observed and the synthetic redshift distribution for clouds with equivalent widths greater than 0.2 Å, the completeness limit for the observed sample. In Figure 5, we plot the redshift distribution for a subsample of clouds with $W_r \geq 0.3$ Å. The normalization for the model curves is fixed by the choice of $\mathscr{K}_0$ as described previously. As discernible from Figure 5 and to a lesser extent, from Figure 4, the total number of simulation clouds seen over the redshift range under consideration is less than the number of observed Lyα clouds. This discrepancy arises because the observed and the synthetic sample, though subjected to the same equivalent width selection criterion, have different column density distributions as a result of the differences in the distribution of the velocity parameters for the two samples—the mean velocity parameter for the absorption profiles associated with the simulated clouds is $\langle b \rangle \approx 22$ km s^{-1} with 1 σ dispersion of $\sigma_b \approx 1$ km s^{-1}, while the mean velocity parameter for the observed profiles is $\langle b \rangle \approx 35$ km s^{-1} with a dispersion of $\sigma_b \approx 15$ km s^{-1} (in agreement with Webb & Carswell 1991; Rauch et al. 1992). The equivalent width of an absorption profile due to a given column density of neutral gas is greater if the associated velocity parameter is larger; hence, an equivalent width–limited sample containing clouds with larger velocity parameters probes down to lower column densities than a sample of clouds with low b. Given the column density distribution for the clouds (e.g., Fig. 3), it is clear that the sample with a lower column density threshold will contain more clouds. Furthermore, the steepness and the sudden truncation of the synthetic $d\mathscr{N}/dN_{\rm H\,I}$ at large column densities also contributes to the discrepancy. It should be noted that the number deficiency at $W_r = 0.2$ Å is minimal because both of the above-mentioned effects are relatively weak: the value of the minimum column density, according to the curve of growth, is relatively insensitive to the value of the velocity parameter and the threshold column densities are small enough that the total number of clouds in the synthetic sample is not greatly affected by the behavior of the $d\mathscr{N}/dN_{\rm H\,I}$ at large column densities. At the higher equivalent width threshold of $W_r = 0.3$ Å, however, the column density threshold is larger and is more sensitive to the value of the velocity parameters of the clouds. Consequently, the discrepancy in the number of synthetic and observed clouds at each redshift is worse. In summary, it is fair to con-

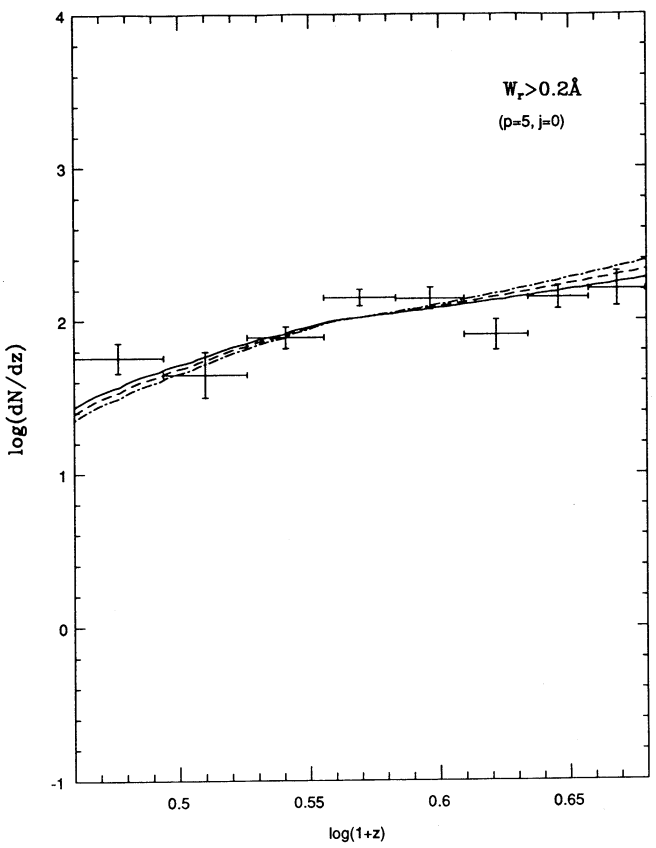

FIG. 4a

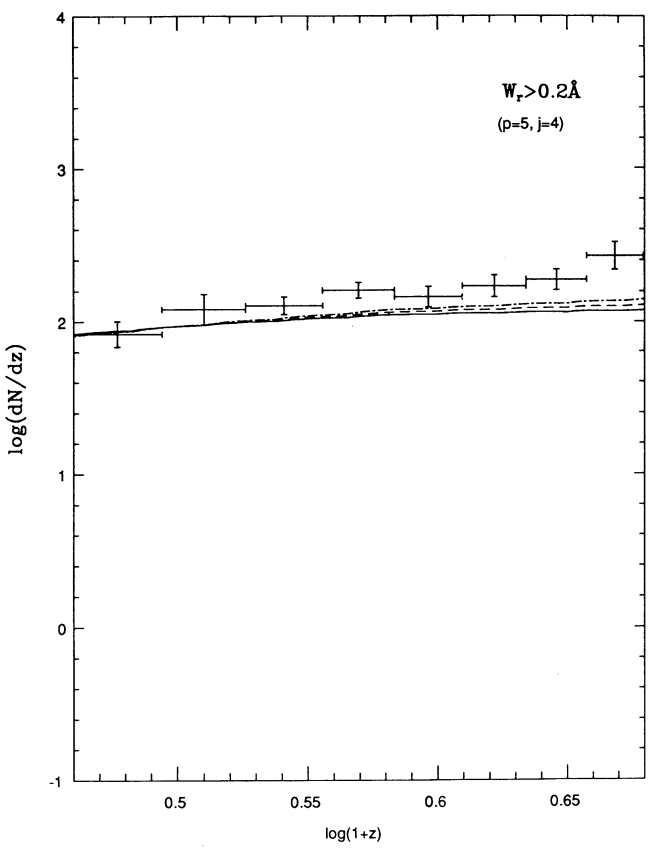

FIG. 4b

FIG. 4.—The observed redshift distribution of Lyα clouds with $W_r \geq 0.2$ Å juxtaposed with the curve corresponding to $d\mathscr{N}/dz$ for pressure-confined clouds also subject to $W_r \geq 0.2$ Å. The model curve corresponds to clouds with mass spectra characterized by $\delta = 1.87$, $\delta = 1.90$, and $\delta = 1.93$. The error bars represent 1 σ errors for the observations. (*a*) shows the results for the $j = 0$ model, and (*b*) shows the results for the $j = 4$ model. The computed redshift density is not, in general, a power-law distribution.

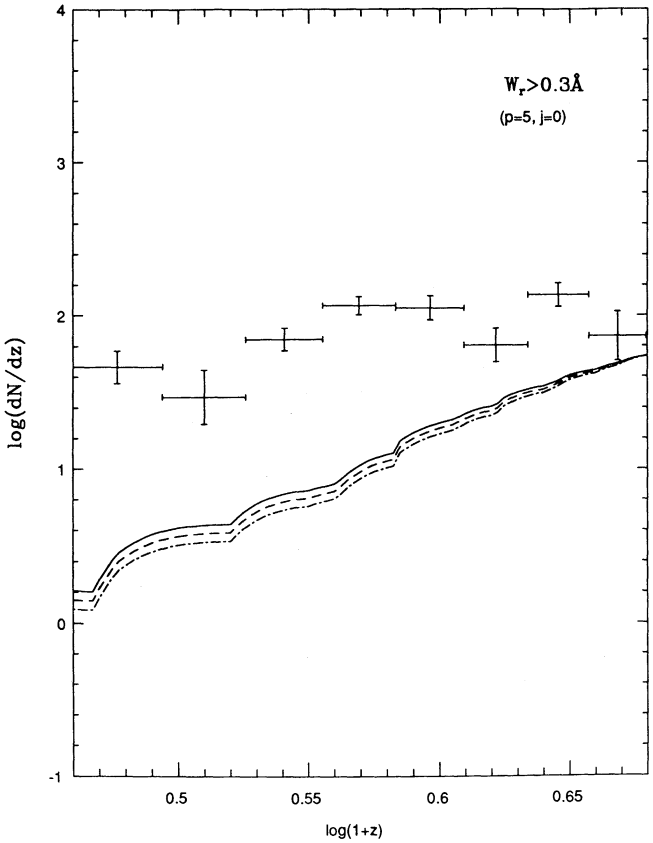

FIG. 5a

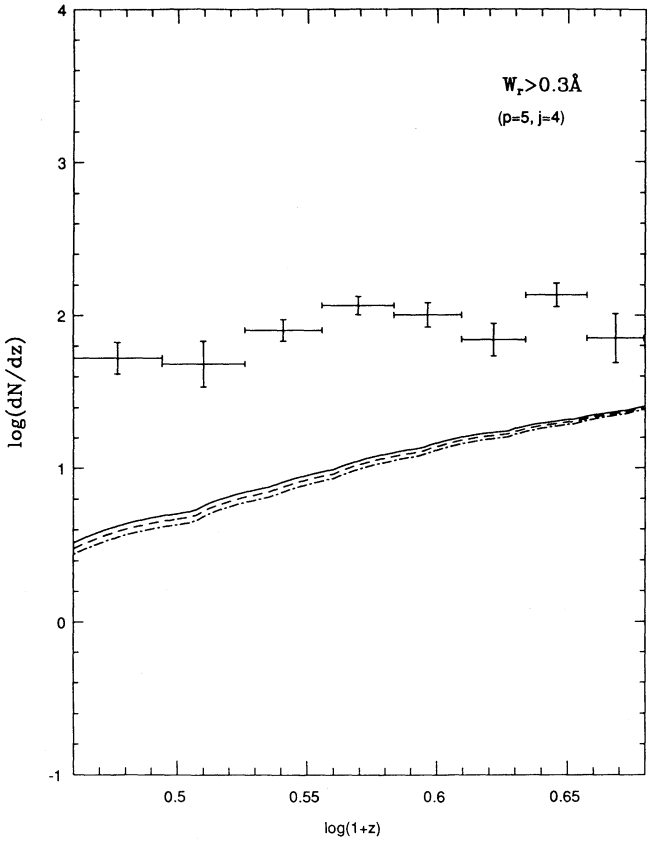

FIG. 5b

FIG. 5.—The redshift density of the clouds, observed and computed, with rest frame equivalent width $W_r \gtrsim 0.3$ Å. The model curves corresponds to clouds with mass spectra characterized by $\delta = 1.87$, $\delta = 1.90$, and $\delta = 1.93$. The error bars represent 1 σ errors for the observations. (*a*) shows the results for the $j = 0$ model, and (*b*) shows the results for the $j = 4$ model.

clude that if the model velocity parameter distribution is inconsistent with that for the observed clouds, it is not possible to normalize simultaneously both the column density distributions and the equivalent width–limited redshift density, even if the functional form of the predicted and the observed distributions were similar.

According to the above discussion, if the observed distribution of b parameters for the Lyα clouds represents the true distribution, then the observed Lyα clouds cannot be pressure-confined entities. However, it is quite possible that the intrinsic distribution of b parameters for Lyα clouds is consistent with the distribution for the synthetic clouds and that the observed distribution is a consequence of distortions introduced by clustering and blending of Lyα lines. Such line blending arises when two close lines, both of which correspond to low-b parameters, are counted as one line with a large velocity parameter. To illustrate this possibility, Carswell et al. (1991) have found that absorption lines with $b \geq 20$ km s^{-1} along the line of sight to Q1100−264 can be fitted by a large number of $b = 13$ km s^{-1} lines. The fact that Lyα lines appear to be weakly clustered on small scales (cf. Babul 1991 and references therein) means that line blending is likely to be an important effect; in fact, clustering on the scale of 20–30 km s^{-1} is quite capable of increasing the mean velocity parameter from 22 to 35 km s^{-1} as well as broadening the distribution (Webb 1991). Since our synthetic distribution does not take into account the above effects, it is not possible, at present, to draw any conclusions based on the differences between it and the observed distribution, or about any effects (such as the discrepancy in the normalization of $d\mathcal{N}/dz$) that arises as a result.

A further study of Figures 4 and 5 reveals that the synthetic curves are not power-law functions expected from the simple theoretical analysis (eq. [14b]): The curves in the figures tend to steepen with decreasing redshift, and, in fact, the redshift density of the pressure-confined clouds declines much too rapidly to account for the observations. For the $\delta = 1.90$ mass spectrum, for example, the $j = 0$ curve corresponding to the $W_r \geq 0.2$ Å sample (Fig. 4*a*) has an effective power index of $\gamma_{\rm eff} \approx 4.1$ at the high-redshift end of the epoch of observation and steepens to $\gamma_{\rm eff} \approx 6.2$ toward the low-redshift end. The redshift index for the observations is $\gamma = 2.21 \pm 0.57$. The discrepancy is even worse for the $W_r \geq 0.3$ Å sample (Fig. 5*a*): The observations correspond to $\gamma = 1.38 \pm 0.59$ while the effective index for the synthetic curve is $\gamma_{\rm eff} \approx 5.7$ at the high-redshift end and steepens rapidly; for example, $\gamma_{\rm eff} \approx 7.775$ over the interval $2.8 \leq z \leq 3.3$. Line blending effects, invoked in the previous paragraph as possible sources of the discrepancy between distributions of the observed and the synthetic velocity parameters, are not likely to account for the flatness (vis-à-vis the synthetic redshift density) of the observed $d\mathcal{N}/dz$ at low redshifts. Babul (1991) has shown that blending of lines causes the "observed" distribution to appear flatter than the actual

TABLE 2

MINIMUM DETECTABLE MASS[a] OF PRESSURE-CONFINED CLOUDS FOR $W_r \geq 0.2$ Å AND $W_r \geq 0.3$ Å SAMPLES

$W_r^{\lim}$	j	$\log [M_L(z)/M_\odot]\|_{z=4}$	$F(z)^b\|_{z=4}$	$\log [M_L(z)/M_\odot]\|_{z=2}$	$F(z)^b\|_{z=2}$
0.2.....	0	2.75	0.97	7.50	0.61
0.3.....	0	4.75	0.91	9.00	0.13
0.2.....	4	4.75	0.91	6.75	0.74
0.3.....	4	6.50	0.77	8.50	0.33

[a] For clouds with mass spectrum $\delta = 1.90$.
[b] $F(z) = 1 - [M_H/M_L(z)]^{-(\delta - 5/3)}$ and $\log (M_H/M_\odot) = 9.25$.

underlying $d\mathcal{N}/dz$ only at high redshifts ($z \gtrsim 2.8$); blending effects would not moderate the rapid decline in the number of clouds towards the present.

According to equation (14b), the "ideal" $j = 0$ curve is a single power law with $\gamma = 3.5$, regardless of the limiting equivalent width of the sample. However, as shown in Table 2, the assumption underlying this "ideal" redshift distribution, that $M_H/M_L(z) \gg 1$ over the entire epoch of observation, is not valid. The synthetic curve is not a power law function because the neglected factor $F(z) = 1 - [M_H/M_L(z)]^{-(\delta - 5/3)}$ takes on values significantly less than unity as $M_L(z)$ approaches M_H at low redshifts. The synthetic curves for the standard ($j = 4$) model is also subject to similar effects. According to equation (14b), the "ideal" redshift density for clouds with mass spectrum $\delta = 1.90$ is a $\gamma = 0.7$ power law. Such a curve would be marginally consistent with the $W_r \geq 0.2$ Å and $W_r \geq 0.3$ Å data samples, which corresponds to $\gamma = 2.00 \pm 0.50$ and $\gamma = 1.36 \pm 0.57$, respectively. The effective redshift index of the $d\mathcal{N}/dz$ distribution for the $W_r \geq 0.2$ Å sample (Fig. 4*b*) is comparable to the analytic value at the high-redshift end, $\gamma_{\rm eff} \approx 0.72$ over the redshift range $3.73 \leq z \leq 3.90$, and gradually steepens to $\gamma_{\rm eff} \approx 1.07$ at the low-redshift end. Based on these results, it can be argued that the synthetic $d\mathcal{N}/dz$ curve for the standard model is quite compatible with the observations if the redshift distribution were appropriately normalized; however, the results for the $W_r \geq 0.3$ Å sample (Fig. 5*b*) paint a different picture. The synthetic curve is considerably steeper than the observed redshift density: $\gamma_{\rm eff} \approx 3$ over the redshift range $3.36 \leq z \leq 3.68$ and increases with decreasing redshift. The results for the $W_r \geq 0.2$ Å and the $W_r \geq 0.3$ Å samples together argue that neither the $j = 0$ nor the standard $j = 4$ models are consistent with the observations.

4.3. *Evolution of* $M_H/M_L(z)$

In the above subsections, we have identified the squeezing of the mass range $M_L(z) \leq M \leq M_H$ for observable clouds with decreasing redshift as the most important source of discrepancy between the observations and the synthetic $d\mathcal{N}/dN_{\rm H\,I}$ and $d\mathcal{N}/dz$ distributions for the pressure-confined model. For example, the steepness of the synthetic $d\mathcal{N}/dz$ for $W_r \geq 0.3$ Å sample (Fig. 5), as compared to both the power law expected from simple analytic considerations and the observations, is the consequence of the factor $F(z)$ becoming significantly smaller than the ratio $M_H/M_L(z)$ and dropping below 1000 (for $\delta \approx 1.9$), as shown in Table 2. In Figure 6, we show the evolution of this ratio for the $W_r \geq 0.3$ Å, as deduced from our simulation results. For the $j = 4$ model, the value of $M_H/M_L(z)$ is less than 1000 over the entire redshift range of interest; this explains why the effective redshift index for the corresponding $d\mathcal{N}/dz$ curve ($\gamma \gtrsim 3$) is much larger than the theoretical value ($\gamma = 0.7$). In the $j = 0$ model, the ratio is initially large, and, hence, the effective redshift index characterizing the synthetic $d\mathcal{N}/dz$ at high redshifts is only sightly larger than the theoretical value. However, the $M_H/M_L(z)$ in this model drops steeply with decreasing redshift, causing the $d\mathcal{N}/dz$ curve to steepen.

In Figure 6, we also plot the theoretical curves for $M_H/M_L(z)$ computed using equations (7) and (13):

$$\frac{M_H}{M_L(z)} = 1.61 \times 10^{-11} (\sqrt{7})^p (3.5)^{3j} (1 + z)^{5p - 3j} . \quad (15)$$

We note that the magnitude of M_H has been adjusted to take into account the fact that the upper mass limit in our simulations is a factor of 4 smaller than the value given by equation

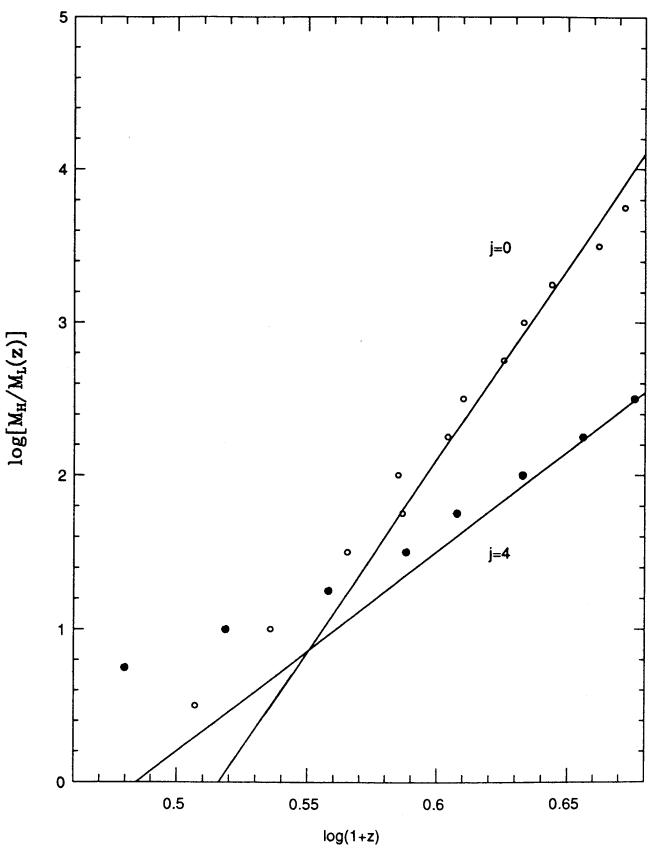

FIG. 6.—The evolution of ratio $M_H/M_L(z)$ with time (decreasing redshift). The open and the filled circles correspond to simulation results for $j = 0$ and $j = 4$, respectively. The two lines trace the evolution of the ratio expected from theoretical considerations. At redshifts $z \gtrsim 2.6$, the theoretical curves agree quite well with the simulation results. At lower redshifts, the loci of simulation points tend to flatten somewhat.

(7). Furthermore, in order to compute the theoretical value of M_L, we use $N_{HI}^{lim} = 10^{14.47}$ cm^{-2}, the threshold column density for our synthetic $W_r \geq 0.3$ Å sample. The theoretical curves and the simulation results are in good agreement at redshifts $z \gtrsim 2.6$ but at lower redshifts, the simulation results suggest that $M_H/M_L(z)$ is not decreasing as rapidly as suggested by equation (15). According to this equation, there ought to be no observable clouds in the $j = 0$ model at redshifts $z \lesssim 2.3$ [$F(z) = 0$]. The discrepancy between the simulation results and the theoretical curve arises because the evolution of $M_L(z)$, as described in equation (13), is based on the assumption that the clouds are always in pressure equilibrium with the ICM. This is certainly true for small clouds, at least over the redshift range of interest to us. At redshifts $z \lesssim 2.6$, however, $M_L(z)$ corresponds to the masses of large clouds, clouds which are tending toward the free expansion phase and hence, not evolving as rapidly.

It is possible that much of the incompatibility between the observations and the pressure-confined Lyα clouds model is due to our assumption that the ICM pressure evolves adiabatically. If the origin of the Lyα clouds is in fragmenting shells associated with cosmological explosions, then the evolution of the ICM pressure experienced by clouds corresponds to $p = 3.6$ (Ikeuchi & Ostriker 1986); the heating of the ICM by shocks associated with gravitational collapse (Cen et al. 1990) will also lead to a nonadiabatic evolutionary scenario where $p < 5$. In spite of the discrepancy between the theoretical curve for $M_H/M_L(z)$ and the simulation results at low redshifts, we can use equation (15) to place limits on the allowed parameter space for (p, j). For the synthetic results to be consistent with the observations, we require that the $d\mathcal{N}/dN_{HI}$ and $d\mathcal{N}/dz$ distributions be more or less simple power laws over the redshift range $1.8 \lesssim z \lesssim 3.8$ and that the associated redshift index be $\gamma \approx 2$. For the synthetic $d\mathcal{N}/dz$ curves associated with $W_r \gtrsim 0.3$ Å, these requirements constrain $M_H/M_L(z)$ to be greater than 1000 and the combination of p and j be such that $0.5p - 0.7j \approx 1$; in deriving these conditions, we have assumed that the mass spectrum of the clouds is characterized by $\delta = 1.9$. Adopting $z = 2.6$ as our fiducial redshift—equation (15) only traces the simulation results for $z \gtrsim 2.6$—we find that the above two conditions imply that $p \gtrsim 5.8$.

5. CONCLUSIONS

In order to investigate the pressure-confined model for the Lyα clouds, we have studied their evolution using a hydrodynamic code and have used the simulation results to construct synthetic column density and redshift density distributions for comparison with observed trends determined using a large, high-resolution profile–fitted dataset. The clouds in our simulations were assumed to be spherically symmetric and optically thin. Further, we assumed that the pressure of the intercloud medium evolves as $P \propto (1 + z)^p$, where $p = 5$, and considered two different models for the evolution of the background ionizing flux: $J_\nu \propto (1 + z)^j$, $j = 0$ and 4. The following conclusions can be drawn from the discussion in the preceding section:

1. In order to reproduce the observed column density distribution over column densities $\log (N_{HI}) \lesssim 15.5$, the mass spectrum of spherical pressure-confined clouds is $d\mathcal{N} \propto M^{-\delta} dM$, $\delta \approx 1.9$.

2. As a result of the upper limit to the mass of the pressure-confined clouds, the mass range for observable clouds is finite and decreases with decreasing redshift. This results in a deficiency of high column density systems, especially at low redshifts, leading to a steepening of the redshift-integrated $d\mathcal{N}/dN_{HI}$ at large N_{HI}. We also examined the column density distribution in a restricted redshift range around $z \approx 2.7$ and found the steepening to be more pronounced. We expect this tendency to grow at lower redshifts. The observed distribution shows no such trends. While inhomogeneities in the ICM pressure can potentially rectify this problem, Webb & Barcons (1991) have argued that such fluctuations in $\Delta P/P$ would also produce detectable correlations in the data, which are not observed.

3. As a result of the fixed upper bound to the mass range for observable clouds, the column density distributions at any specific redshift exhibit a sharp cutoff. At $z \approx 2.7$, no clouds are seen beyond $\log (N_{HI}) = 17.8$ for $j = 0$ and $\log (N_{HI}) = 15.6$ for $j = 4$. The cutoff is in conflict with the observations.

4. We find that the distribution of velocity parameter for our simulated clouds has a mean of 22 km s^{-1} with very little dispersion, while the corresponding distribution for the observed clouds has a mean of 35 km s^{-1} with a dispersion of 15 km s^{-1}. As a result of this discrepancy, the total number of simulated clouds in a sample selected using the rest frame equivalent width as a detection criterion is much smaller than the number of observed clouds, especially if the threshold is as high as $W_r = 0.3$ Å. It is possible that the intrinsic velocity parameter distribution of Lyα clouds is similar to our synthetic one but the observed distribution arises due to distortions caused by line blending effects.

5. The finite and varying—decreasing with time—mass range for observable clouds also affects the redshift density distribution of synthetic clouds. The synthetic redshift densities of clouds tend to decrease much more rapidly than observed. A sample subject to the $W_r \geq 0.3$ Å detection criterion is more severely affected than that subject to a lower threshold limit. In passing, we note that *HST* observations by Morris et al. (1991) suggest that there are more clouds at very low redshift than expected using power-law extrapolations from optically observed redshifts; such a trend is very much the opposite of that predicted by the pressure-confined model.

On the basis of our results, we find that the spherically symmetric pressure-confined clouds model is inconsistent with the observations. It can be argued that other choices for the parameters p and j may alleviate the disagreements between the observations and the model. However, the crux of the problem with the pressure-confined model is the extremely limited mass range for observable clouds, a mass range that rapidly decreases with time. In order to expand the mass range and simultaneously satisfy the dynamical constraints as well as the observations, we find that p must be greater than 5.8; it is difficult to envision how a uniform ICM pressure can decrease faster than adiabatic, especially over the epoch when gravitational collapse is more likely to be heating the gas. To reiterate, our findings suggest that spherical clouds are not suitable candidates for the observed Lyα clouds; however, it is possible that aspherical pressure-confined clouds may yield better agreement with observations. In fact, Baron et al. (1989) have implied that sheetlike pressure-confined clouds would allow for observations of high column density systems at low redshifts. Furthermore, it is much more likely that clouds originating in fragmenting shells associated with shock waves evolve aspherically, becoming increasing oblate with time (Thompson 1990).

The authors acknowledge helpful discussions with R. F.

Carswell, M. J. Rees, J. P. Ostriker, J. K. Webb, R. Duncan, J. A. Baldwin, and A. Meiksin. The line profiles for the simulated clouds were computed using R. Weymann's software. We are indebted to him. During the course of this work, G. M. W. received support from Jesus College, Cambridge, while A. B. was primarily supported by a NATO Science Fellowship. G. M. W. is grateful for the hospitality shown to him by the Canadian Institute for Theoretical Astrophysics.

REFERENCES

Atwood, B., Baldwin, J. A., & Carswell, R. F. 1985, ApJ, 292, 58
Babul, A. 1991, MNRAS, 248, 177
Bajtlik, S., Duncan, R. C., & Ostriker, J. P. 1988, ApJ, 327, 570
Baron, E., Carswell, R. F., Hogan, C. J., & Weymann, R. J. 1989, ApJ, 337, 609
Bechtold, J., Weymann, R. J., Lin, Z., & Malkan, M. A. 1987, ApJ, 315, 180
Bergeron, J. 1988, in Quasar Absorption Lines: Probing the Universe, ed. J. C. Blades, C. Norman, & D. Turnshek (Cambridge: Cambridge Univ. Press), 127
Black, J. H. 1981, MNRAS, 197, 553
Blades, J. C. 1988, in Quasar Absorption Lines: Probing the Universe, ed. J. C. Blades, C. Norman, & D. Turnshek (Cambridge: Cambridge Univ. Press), 147
Carr, B. J., Bond, J. R., & Arnett, W. D. 1984, ApJ, 277, 445
Carswell, R. F. 1990, private communication
Carswell, R. F., Lanzetta, K. M., Parnell, H. C., & Webb, J. K. 1991, ApJ, 371, 36
Carswell, R. F., Morton, D. C., Smith, M. G., Stockton, A. N., Turnshek, D. A., & Weyman, R. J. 1984, ApJ, 278, 486
Carswell, R. F., Robertson, J. G., Shaver, P. A., & Webb, J. K. 1992, in preparation
Carswell, R. F., Webb, J. K., Baldwin, J. A., & Atwood, B. 1987, ApJ, 319, 709
Cen, R. Y., Jameson, A., Liu, F., & Ostriker, J. P. 1990, ApJ, 362, L41
Chaffee, F. H., Jr., Foltz, C. B., Bechtold, J., & Weymann, R. J. 1986, ApJ, 301, 116
Cowie, L. L., & McKee, C. F. 1977, ApJ, 211, 135
Duncan, R. C., & Ostriker, J. P. 1988, Preprint, POP-261
Evans, A., & Hart, D. 1977, A&A, 58, 241
Ikeuchi, S. 1987, in High Redshift & Primeval Galaxies, ed. J. Bergeron, D. Kunth, B. Rocca-Volmerange, & J. Tran Thanh Van (Gif sur Yvette: Editions Frontières), 485
Ikeuchi, S., Murakami, I. & Rees, M. J. 1989, MNRAS, 236, 21P
Ikeuchi, S., & Ostriker, J. P. 1986, ApJ, 301, 522
Lu, L. 1991, ApJ, 379, 99
Lu, L., Wolfe, A. M., & Turnshek, D. A. 1991, ApJ, 367, 37
Meyer, D. M., & York, D. G. 1987, ApJ, 315, L5
Morris, S. L., Weymann, R. J., Savage, B. D., & Gilliland, R. L. 1991, ApJ, 377, L1
Murdoch, H. S., Hunstead, R. W., Pettini, M., & Blades, J. C. 1986, ApJ, 309, 19
Ostriker, J. P. 1988, in Quasar Absorption Lines: Probing the Universe, ed. J. C. Blades, C. Norman, & D. Turnshek (Cambridge: Cambridge Univ. Press), 320
Ostriker, J. P., & Cowie, L. L. 1981, ApJ, 243, L127
Ostriker, J. P., & Ikeuchi, S. 1983, ApJ, 268, L63
Rauch, M., Carswell, R. F., Chaffee, F. H., Foltz, C. B., Webb, J. K., Weymann, R. J., Bechtold, J., & Green, R. F. 1992, ApJ, 390, 387
Rauch, M., Carswell, R. F., Robertson, J. G., Shaver, P. A., & Webb, J. K. 1990, MNRAS, 242, 698
Rees, M. J. 1986, MNRAS, 218, 25P
———. 1988, in Quasar Absorption Lines: Probing the Universe, ed. J. C. Blades, C. Norman, & D. Turnshek (Cambridge: Cambridge Univ. Press), 107
Sargent, W. L. W. 1988, in Quasar Absorption Lines: Probing the Universe, ed. J. C. Blades, C. Norman, & D. Turnshek (Cambridge Univ: Press), 1
Sargent, W. L. W., Young, P. J., Boksenberg, A., & Tytler, D. 1980, ApJS, 42, 41
Schneider, D. P., Schmidt, M. & Gunn, J. E. 1989, AJ, 98, 1951
Thompson, C. 1990, in IAU Symp. 140, Galactic and Intergalactic Magnetic Fields, ed. R. Beck, P. P. Kronberg, & R. Wielebinski (Dordrecht: Kluwer), 507
Tytler, D. A. 1987, ApJ, 321, 69
———. 1988, in Quasar Absorption Lines: Probing the Universe, ed. J. C. Blades, C. Norman, & D. Turnshek (Cambridge: Cambridge Univ. Press), 179
Umemura, M., & Ikeuchi, S. 1984, Prog. Theor. Phys., 72, 47
Vishniac, E. T. 1983, ApJ, 274, 152
Vishniac, E. T., Ostriker, J. P., & Bertschinger, E. 1985, ApJ, 291, 399
Webb, J. K. 1987a, PhD. thesis, Cambridge University
———. 1987b, in IAU Symp. 124, Observational Cosmology, ed. A. Hewitt, G. Burbidge, & Li-Zhi Fang (Dordrecht: Reidel), 803
———. 1991, private communication
Webb, J. K., & Barcons, X. 1991, MNRAS, 250, 270
Webb, J. K., & Carswell, R. F. 1991, in Procs ESO Mini-Workshop on Quasar Absorption Lines (ESO Report 9), ed. P. A. Shaver, E. J. Wampler, & A. M. Wolfe (Garching bei München: ESO), 3
Williger, G. M. 1991, Ph.D. thesis, Cambridge University